Implementation of the Critical Unstable Condition in Extended Finite-Element Analysis to Calculate the Safety Factor of a Predefined Slip Surface

Lu Shi[1]; Bing Bai[2]; and Xiaochun Li[3]

Abstract: This study incorporated the critical unstable condition into extended finite-element analysis to determine the safety factor of a slip surface that is regarded as a discontinuity embedded into the slope mesh. The displacement field and the safety factor can be obtained simultaneously by directly solving the final nonlinear equations. Moreover, the augmented Lagrange multiplier method and the vital vertex algorithm were used to improve the accuracy of the normal stress on the slip surface. Three examples were presented to demonstrate various aspects of the proposed method, including its efficiency in searching for the critical slip surface without remeshing and sensitivity to the finite-element mesh. **DOI:** [10.1061/(ASCE)GM.1943-5622.0001356.](#) © *2018 American Society of Civil Engineers.*

Introduction

Stability analyses should be performed routinely to assess the safe design of a slope or to provide possible remedy measures for an unstable slope (Eberhardt 2003; de Vallejo and Ferrer 2011). The stability analysis of a slope usually involves the calculation of the factor of safety (FOS, F_s), which should be greater than 1 for a stable slope.

One method of obtaining the safety factor is to divide the total resisting force by the total driving force, and these can be determined by integrating the shear strength and shear stress along the slip surface. The stress state on the slip surface can be determined by finite-element analysis (FEA) (Brown and King 1966; Kulhawy 1969; Naylor 1982; Fredlund et al. 1999; Liu et al. 2015). Additionally, the stress direction can vary on the slip surface, and the physical meaning of the total stress in integral form is unclear when the slip surface is not circular or planar. To overcome this limitation, Ge et al. (1995) projected the stress of the slip surface in the principal sliding direction and proposed the vector summation method to calculate the total resisting and sliding forces; this method was subsequently improved and applied in other studies (Ge 2010; Shi et al. 2012; Fu et al. 2017). However, the concept of

the principal sliding direction remains unclear, and this parameter may vary based on different methods.

A second approach used to determine the safety factor is to simultaneously reduce the shear strength of the entire slope or slip surface by a certain factor (F_s) to create a limit equilibrium state (i.e., after decreasing the shear strength, the shear stress at each point on the slip surface is equal to the shear strength). The strength-reduction method (SRM), which has been implemented in FEA (Zienkiewicz et al. 1975; Donald and Giam 1988; Matsui and San 1992; Griffiths and Lane 1999; Dawson et al. 1999; Bai et al. 2014), and the limit-equilibrium method (LEM) (Bishop 1955; Morgenstern and Price 1965; Spencer 1967; Janbu 1975) are the two primary methods of calculating the safety factor in this approach. The LEM is used by most engineers due to its simplicity. To force the slope-stability calculation to be a determinant problem, assumptions regarding the interslice forces are used in the LEM without a theoretical basis; these assumptions may influence the F_s solution for the slip surface. In addition, as a method of force analysis for a rigid body, the actions of the stabilization measures and overloads are usually simplified in the LEM because the deformation behavior of the slope materials cannot be considered. With the aid of stress–strain analysis in FEA, the SRM can overcome the aforementioned deficiencies of the LEM and automatically locate the critical slip surface (CSS), which is the slip surface that yields the minimum F_s, without a trial-and-error search (Zheng et al. 2005; Wang et al. 2016). Because the SRM is used to reduce the shear strength of the whole slope, determining the other slip surfaces of interest, which are slightly less critical than the CSS, is difficult; these surfaces may also require treatment in engineering practice (Cheng et al. 2007; Cheng and Lau 2014). Furthermore, the selection of the instability criterion also influences the solution of the SRM. Both the LEM and the SRM have advantages and disadvantages. Therefore, we introduced the critical unstable condition of the prescribed slip surface into FEA and proposed a FEA-based limit-equilibrium (FELE) method for evaluating the stability of the predefined slip surfaces. The safety factor and displacement field can be simultaneously determined in the FELE method (Shi et al. 2017). As with the traditional LEM, the FELE method must be combined with a global optimization technique to locate the CSS of

[1]Associate Professor, State Key Laboratory of Geomechanics and Geotechnical Engineering, Institute of Rock and Soil Mechanics, Chinese Academy of Sciences, Wuhan, Hubei 430071, China (corresponding author). ORCID: https://orcid.org/0000-0002-2040-5895. Email: shilu .whrsm@qq.com

[2]Associate Professor, State Key Laboratory of Geomechanics and Geotechnical Engineering, Institute of Rock and Soil Mechanics, Chinese Academy of Sciences, Wuhan, Hubei 430071, China. Email: bai_bing2@ 126.com

[3]Professor, State Key Laboratory of Geomechanics and Geotechnical Engineering, Institute of Rock and Soil Mechanics, Chinese Academy of Sciences, Wuhan, Hubei 430071, China. Email: xcli@whrsm.ac.cn

the slope. Therefore, the calculation of the safety factor of each slip surface must be as simple as possible because optimization algorithms usually require many trial calculations (Kim and Lee 1997; Pham and Fredlund 2003; Shi et al. 2009). However, a shortcoming of the FELE method is that the mesh must be reconstructed for each potential slip surface, which is detrimental to the efficient determination of the CSS. Because the FELE approach regards the slip surface as a discontinuity, a change in the slip surface can be treated as a moving discontinuity.

Many methods have several advantages in modeling moving discontinuity problems, among which the extended FEA (XFEA), pioneered by Belytschko and Black (1999) and Moës et al. (1999), has been widely applied for crack propagation in solid mechanics (Sukumar et al. 2000; Giner et al. 2009; Chin et al. 2017). With discontinuous interpolation functions in the framework of the partition of unity method (Melenk and Babuška 1996), XFEA treats the discontinuities as independent of the finite-element mesh and circumvents the requirement of conforming the mesh to the discontinuities in the standard FEA. Therefore, XFEA has superiority in simulating moving discontinuity without updating the mesh. The original XFEA can only be used to solve the problem of single crack propagation under tensile stress. After more than a decade of rapid development, XFEA is now capable of solving problems involving intersections of multiple cracks (Daux et al. 2000; Budyn et al. 2004; Zhou and Yang 2012; Zhou and Cheng 2017). Furthermore, many methods have been adopted in XFEA to study the contact between crack surfaces; these studies included the large time increment method (Dolbow et al. 2001), conventional penalty method (Khoei and Nikbakht 2007; Liu and Borja 2009), updated Lagrangian formulation (Khoei et al. 2009), total Lagrangian formulation (Zhou and Cheng 2017), and augmented Lagrangian multiplier method (Shi and Yu 2014; Hirmand et al. 2015). For the complex contact problems including multiple contact states on a crack, Cheng and Zhou (2018) developed an effective technique with 10 equally spaced points on the cracks to detect the contact state in the framework of XFEA. Moreover, to avoid variations in the number of degrees of freedom (DOFs) with the growth of cracks, which can lead to difficulties in the iterative algorithm of time integration, the multidimensional space method with all nodes in the computational domain enriched was proposed by Cheng and Zhou (2015).

To search for the CSS without remeshing the slope based on the FELE concept, this study replaced FEA with XFEA due to its advantages in modeling moving discontinuity. To facilitate the search for the CSS, the proposed method uses a triangular mesh, in which each node has four DOFs, including two standard DOFs and two enhanced DOFs. This approach is similar to the multidimensional space method, and each triangle has three subregions for numerical integration. Thus, the data structure of the mesh remains unchanged when evaluating the stability of different slip surfaces. By exploiting the advantages of XFEA, the improved method is computationally efficient in locating the CSS without reconstructing the mesh of the slope under evaluation. In this paper, several examples are given to illustrate the utility and effectiveness of the proposed method.

Governing Equations of the Stability Analysis of a Given Slip Surface

Boundary Value Problem

Consider a discontinuity Γ_d (slip surface) in domain Ω (slope) with boundary Γ, as presented in Fig. 1. The domain is divided into Ω^+ (sliding body) and Ω^- (sliding bed) by Γ_d. The side of Γ_d within Ω^+
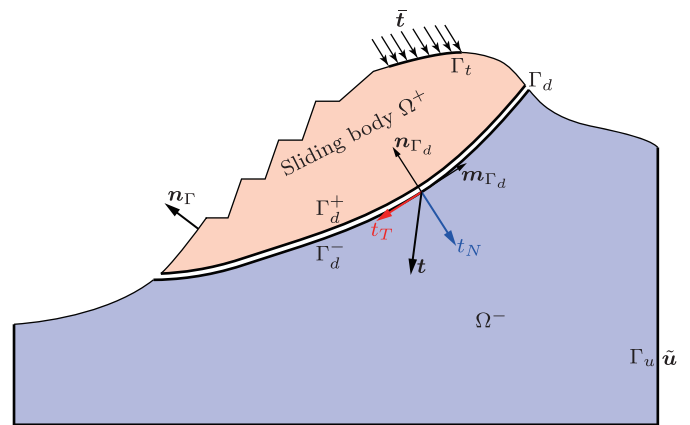

Fig. 1. Definition of a two-dimensional slope with a slip surface requiring evaluation.

is called the positive side (Γ_d^+), and the other side is called the negative side (Γ_d^-). The static equilibrium equation in Ω is as follows:

$$\nabla \cdot \boldsymbol{\sigma} + \mathbf{b} = 0 \qquad (1)$$

where $\boldsymbol{\sigma}$ = Cauchy stress tensor; $\mathbf{b}$ = body force vector; and ∇ = vector gradient operator. The stress tensor ($\boldsymbol{\sigma}$) can be related to the strain tensor ($\boldsymbol{\epsilon}$) using a constitutive equation. In this study, the behavior of the slope body material was assumed to be linear elastic, and the constitutive equation can be represented by $\boldsymbol{\sigma} = \mathbf{D} : \boldsymbol{\epsilon}$, where $\mathbf{D}$ denotes the fourth-order elastic tensor.

The displacement boundary condition is $\mathbf{u} = \tilde{\mathbf{u}}$ on $\Gamma_u \subset \Gamma$, where $\mathbf{u}$ is the displacement variable of the slope, and $\tilde{\mathbf{u}}$ is the prescribed displacement at the displacement boundary (Γ_u). The traction boundary condition is $\boldsymbol{\sigma} \cdot \mathbf{n}_\Gamma = \bar{\mathbf{t}}$ on $\Gamma_t \subset \Gamma$, where $\mathbf{n}_\Gamma$ is the unit outward normal vector of the external boundary (Γ), and $\bar{\mathbf{t}}$ is the prescribed traction on boundary Γ_t. At each node located on Γ, either the displacement or traction must be prescribed (i.e., $\Gamma_u \cap \Gamma_t = \varnothing$ and $\Gamma_u \cup \Gamma_t = \Gamma$).

Moreover, the domains Ω^+ and Ω^- interact with each other through the boundary Γ_d. Therefore, the aforementioned boundary value problem should be modified by considering the traction of the discontinuity (i.e., $\boldsymbol{\sigma} \cdot \mathbf{n}_{\Gamma_d} = t_N \mathbf{n}_{\Gamma_d} + t_T \mathbf{m}_{\Gamma_d} \equiv \mathbf{t}$ on Γ_d, where $\mathbf{n}_{\Gamma_d}$ is the unit normal vector of Γ_d pointing toward Ω^+, $\mathbf{m}_{\Gamma_d}$ is the unit tangential vector of Γ_d in the direction opposite the sliding direction, and t_T and t_N are the tangential and normal components of traction, respectively). Thus, the traction is $\mathbf{t}$ on the Γ_d^- side of the discontinuity, and the traction is $-\mathbf{t}$ on the Γ_d^+ side.

To solve the boundary value problem with a discontinuity, Eq. (1) must be transformed into a weak form by multiplying by a virtual displacement ($\delta \mathbf{u}$) and integrating over Ω

$$\int_\Omega \delta \mathbf{u} (\nabla \cdot \boldsymbol{\sigma} + \mathbf{b}) d\Omega = 0 \qquad (2)$$

According to the divergence theorem, Eq. (2) can be written as follows:

$$\int_\Omega \delta \boldsymbol{\epsilon} : \boldsymbol{\sigma} d\Omega + \int_{\Gamma_d} [\delta \mathbf{u}] \cdot \mathbf{t} d\Gamma - \int_{\Gamma_t} \delta \mathbf{u} \cdot \bar{\mathbf{t}} d\Gamma - \int_\Omega \delta \mathbf{u} \cdot \mathbf{b} d\Omega = 0$$

$$(3)$$

where $\delta \boldsymbol{\epsilon} = \frac{1}{2}(\nabla \delta \mathbf{u} + \nabla^T \delta \mathbf{u})$; $[\mathbf{u}]$ = displacement jump along the discontinuity, and $[*] = *^+ - *^-$, where the subscripts $+$ and $-$ denote the variables for Γ_d^+ and Γ_d^-, respectively. The virtual

displacement ($\delta\mathbf{u}$) must be kinematically admissible—that is, it must satisfy the displacement boundary condition.

Normal Contact Constraint

The contact constraint of the slip surface is the nonpenetration condition [i.e., the normal stress (t_N) can develop when $g_N = 0$, where $g_N = [\mathbf{u}] \cdot \mathbf{n}_{\Gamma_d}$ is the gap in the slip surface; otherwise, $t_N = 0$ and $g_n > 0$]. Hence, the mathematical description of the contact constraint can be written as follows:

$$g_N \geq 0, \ t_N \leq 0, \ g_N t_N = 0 \ \forall \mathbf{x} \in \Gamma_d \tag{4}$$

In most cases, the two sides of the slip surface are in full contact with each other, but some of the slip surfaces are open at the tailing portion. Therefore, symbol $\Gamma_d^{\text{cont}} \subset \Gamma_d$ is used to denote the contact region of the slip surface, where $g_N = 0$ and $t_N \leq 0$. In general, the contact state of the slip surface is not known a priori and must be determined by means of an iterative algorithm.

Two schemes are frequently used to introduce the constraint of $g_N = 0$ on Γ_d^{cont} in Eq. (3): the penalty method and the Lagrange multiplier method. Both of these methods have advantages and disadvantages. Therefore, the augmented Lagrange multiplier method (ALM) (Simo and Laursen 1992; Hirmand et al. 2015) is used to impose the constraint. This method combines the advantages of the penalty and Lagrange multiplier methods and not only reduces the ill conditioning of the stiffness matrix but also satisfies the constraint at a higher level. The ALM uses an iterative technique to update the normal stress

$$t_N^{(m+1)} = t_N^{(m)} + k_N g_N^{(m)} \ \forall \mathbf{x} \in \Gamma_d^{\text{cont}} \tag{5}$$

where $k_N \gg 1$ = strictly positive penalty parameter; subscript m = mth step of the ALM; and $t_N^{(0)}$ = known initial normal stress on Γ_d^{cont}. Notably, t_N in Eq. (5) is nearly identical to the augmented Lagrange multiplier (Hirmand et al. 2015), except that it considers the initial condition. In each augmentation step with $t_N^{(m)}$ known, the normal stiffness (k_N) is used to approximate the nonpenetration constraint, which is consistent with the normal penalty factor in the penalty method; the difference is that k_N does not need to be extremely large, as in the penalty method, to improve the accuracy of the ALM solution. A relatively large value of k_N can help the iterative ALM method converge faster; however, the desired level of accuracy of the solution should be independent of k_N. The convergence with respect to k_N and the associated estimation process are discussed in Numerical example 1.

Critical Unstable Condition

The critical unstable condition includes a stress constraint and a tangential displacement jump constraint on the discontinuity (Γ_d).

In the critical unstable state, the shear stress must equal the shear strength after the reduction on Γ_d

$$t_T = \frac{1}{F_s}(t_N \tan\phi - c) \ \forall \mathbf{x} \in \Gamma_d \tag{6}$$

where ϕ and c = friction angle and cohesion, respectively. Eq. (6) is the well-known limit-equilibrium condition. Clearly, the traction on the discontinuity (Γ_d) is related to t_N and F_s only. As can be observed, because all points on Γ_d^{cont} are in the slip state, no special algorithm is required to determine the *slip-slick* state of the slip surface as the general frictional contact problems.

The problem cannot be determined with only the constraint given in Eq. (6), because if only the force equilibrium is satisfied, a sliding body with a circular or planar slip surface can slide any distance under the assumptions of small deformation and perfect plasticity. When the state of the stress on the slip surface changes from the existing conditions to the limit-equilibrium condition, a tangential displacement jump of the slip surface (g_T) should occur in the sliding direction

$$g_T = [\mathbf{u}] \cdot \mathbf{m}_{\Gamma_d} \leq 0 \ \forall \mathbf{x} \in \Gamma_d \tag{7}$$

Moreover, a point that does not undergo a tangential displacement jump on Γ_d must exist; otherwise, the slip body has lost its stability. This point is called the critical unstable point (CUP), and the constraint on this point can be written as follows:

$$g_T = 0 \ \exists \mathbf{x} \in \Gamma_d \tag{8}$$

It follows that the value of t_T at the CUP is not related to g_T but is related to the normal stress at this point and the FOS. Therefore, the FOS must be adjusted so that Eq. (8) can be satisfied. In this case, Eq. (8) serves as a supplementary equation to introduce the unknown of FOS, and the boundary value problem of slip surface stability can be determined based on the conditions of Eqs. (5), (6), and (8). Moreover, Eq. (7) can be used to determine whether the selection of the CUP is correct. The specific determination of the location of the CUP is discussed in the next section.

Modeling of the Slip Surface in the Critical Unstable State with XFEA

XFEA Approximation

To accurately simulate the mechanical behavior of a solid containing discontinuities, nodes must be arranged on the discontinuity in the standard FEA. Therefore, a change in the discontinuity will cause a modification of the mesh topology. This modification is the primary problem associated with searching for the CSS based on the FELE method, in which the mesh must be regenerated for each potential slip surface. Therefore, XFEA based on the partition of unity method was used in this study to discretize the slope and slip surface. The most powerful advantage of this method is that the discontinuity can be independent of the mesh; therefore, the mesh does not require modification when the location of the discontinuity changes. To embed the discontinuity within the mesh, an enrichment function is added to approximate the space with a jump in the displacement field. The enriched displacement field can be written as follows:

$$\mathbf{u}^h(\mathbf{x}) = \sum_{I \in \mathcal{N}} N_I \overline{\mathbf{u}}_I + \sum_{I \in \mathcal{N}^{\text{enr}}} N_I \big(H(\mathbf{x}) - H(\mathbf{x}_I)\big)\overline{\mathbf{a}}_I$$
$$= \mathbf{N}(\mathbf{x})\overline{\mathbf{u}} + \widetilde{\mathbf{N}}(\mathbf{x})\overline{\mathbf{a}} \ \mathbf{x} \in \Omega \tag{9}$$

where $\mathcal{N}$ = set of all nodes; $\mathcal{N}^{\text{enr}}$ = set of nodes enriched by the function $H(\mathbf{x})$ (namely, the support region of the nodes in $\mathcal{N}^{\text{enr}}$ is bisected by the discontinuity); N_I = standard shape function; $\overline{\mathbf{u}}_I = \mathbf{u}(\mathbf{x}_I)$ = vector of the standard nodal displacement of node I; $\overline{\mathbf{a}}_I = \mathbf{a}(\mathbf{x}_I)$ = vector of the enriched DOF of node $I \in \mathcal{N}^{\text{enr}}$; and $H(\mathbf{x})$ = Heaviside function used to model the discontinuity. $H(\mathbf{x})$ can be written as follows:

$$H(\mathbf{x}) = \begin{cases} 1, & \varphi(\mathbf{x}) \geq 0 \\ -1, & \varphi(\mathbf{x}) < 0 \end{cases} \tag{10}$$

with

$$\varphi(\mathbf{x}) = \text{sign}\big(\mathbf{n}_{\Gamma_d}(\mathbf{x}^*) \cdot (\mathbf{x} - \mathbf{x}^*)\big)||\mathbf{x} - \mathbf{x}^*|| \tag{11}$$

where $\varphi(\mathbf{x})$ = signed distance function; $\mathbf{x}^*$ = closest projection of $\mathbf{x}$ on Γ_d; and $||\mathbf{x} - \mathbf{x}^*||$ = distance between $\mathbf{x}^*$ and $\mathbf{x}$. In addition to obtaining the value of the Heaviside function, the calculation of the signed distance of each node to the discontinuity can also be used to determine the location of the discontinuity by solving $\varphi(\mathbf{x}) = 0$. The slip surface is then approximated as a polyline with vertices that are the intersections of the slip surface and the edges of the mesh.

The enrichment function $[H(\mathbf{x}) - H(\mathbf{x}_I)]$ in Eq. (9) is called a shifted-basis enrichment (Ventura et al. 2003; Giner et al. 2009), which is used to set $\overline{\mathbf{u}}_I$, associated with the enriched node (I), equal to the real nodal displacement vector.

According to Eq. (8), the displacement jump on Γ_d can be written as follows:

$$[\mathbf{u}^h] = \mathbf{u}^h(\mathbf{x}^+) - \mathbf{u}^h(\mathbf{x}^-) = 2\mathbf{N}(\mathbf{x})\overline{\mathbf{a}} \ \ \mathbf{x} \in \Gamma_d \tag{12}$$

The strain ($\boldsymbol{\epsilon}$) is also decomposed into standard and enriched parts

$$\overline{\boldsymbol{\epsilon}}^h(\mathbf{x}) = \sum_{I \in \mathcal{N}} \mathbf{B}_I \overline{\mathbf{u}}_I + \sum_{I \in \mathcal{N}^{\text{enr}}} \mathbf{B}_I(H(\mathbf{x}) - H_I)\overline{\mathbf{a}}_I = \mathbf{B}(\mathbf{x})\overline{\mathbf{u}} + \widetilde{\mathbf{B}}(\mathbf{x})\overline{\mathbf{a}} \ \ \mathbf{x}$$

$$\in \Omega \tag{13}$$

where $\mathbf{B}(\mathbf{x}) = \mathbf{L}\mathbf{N}(\mathbf{x})$ and $\widetilde{\mathbf{B}}(\mathbf{x}) = \mathbf{L}\widetilde{\mathbf{N}}(\mathbf{x})$ = strain matrices corresponding to the standard displacement and enriched DOFs, respectively; and $H_I \equiv H_I(\mathbf{x}_I)$. Note that $\mathbf{L}$ represents the differential strain operator, and $\overline{\boldsymbol{\epsilon}}$ is the vector form of the strain tensor ($\boldsymbol{\epsilon}$).

Implementation of the Critical Unstable Condition and Contact Constraint in XFEA

To formulate the discrete form of Eq. (2), the discontinuity must be discretized for numerical integration. In standard FEA, the discontinuity conforms to the mesh and is discretized into nodes or edges. However, the discontinuity and mesh in XFEA are independent. As discussed earlier, the discontinuity (Γ_d) is approximated as a polyline, with each of its segments embedded in an element, as presented in Fig. 2. Therefore, Γ_d can be easily discretized based on the vertices of the polyline, and the contact constraints of Eq. (7) are enforced. However, the adoption of this technique can yield an overconstrained formulation and result in an abnormal oscillation in the calculated stress at the discontinuity (Moës et al. 2006). Hence, the discrete space of the discontinuity must be coarsened, and the stabilization scheme based on the vital vertex technique (VVT), which was proposed by Hirmand et al. (2015), is used. This technique involves two steps: the selection of vital vertices and numerical integration along the discontinuity. The latter is discussed in the following subsection.

The vital vertices are the locations on the discontinuity used to impose the contact constraint, and they are the subset of the vertices on the polyline, as presented in Fig. 2. Furthermore, the values of t_N are stored at the vital vertices, and the values of t_N at the other positions on Γ_d must be interpolated. The assignment of the vital vertices is based on two criteria: (1) a node of the mesh cannot be connected to two vital vertices, and (2) a nonvital vertex must be
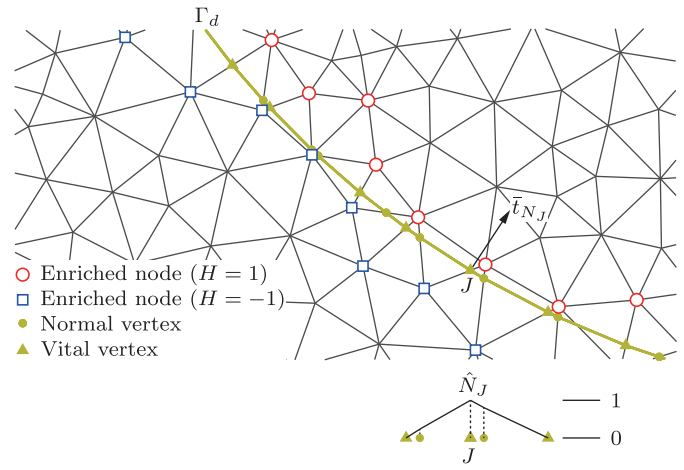

Fig. 2. Discontinuity passing through the triangular mesh and interpolation of the stress on the discontinuity.

connected to a vital vertex through one mesh node. Two criteria are used to ensure that overconstrained and underconstrained formulations are avoided. The specific selection process is as follows: (1) mark all enriched nodes with a *false* flag, and (2) loop over all vertices along Γ_d. When a vertex is connected to two nodes with *false* flags, this vertex is selected as a vital vertex, and the two nodes are marked with *true* flags.

Two adjacent vital vertices and the segments between them form a contact element, and t_N on Γ_d can be approximated as follows:

$$t_N(\mathbf{x}) = \sum_{J \in \mathcal{M}} \widehat{N}_J \overline{t}_{N_J} \equiv \widehat{\mathbf{N}}(\mathbf{x})\overline{\mathbf{t}}_N \ \ \mathbf{x} \in \Gamma_d \tag{14}$$

where $\mathcal{M}$ = set of all vital vertices on Γ_d; and $\widehat{N}_J$ = shape function associated with vital vertex J (Fig. 2). Note that the distance between $\mathbf{x}$ and a vital vertex should be calculated along Γ_d in the calculation of $\widehat{N}_J$.

Substituting Eqs. (5), (6), (9), and (12)–(14) into Eq. (3), the discrete form of Eq. (3) for the mth augmentation iteration can be expressed as follows:

$$\begin{bmatrix} \mathbf{K}_{uu} & \mathbf{K}_{ua} \\ F_s\mathbf{K}_{ua}^{\text{T}} & F_s(\mathbf{K}_{aa} + \mathbf{K}_{cN}) + \mathbf{K}_{cT} \end{bmatrix} \begin{Bmatrix} \overline{\mathbf{u}} \\ \overline{\mathbf{a}} \end{Bmatrix}^{(m)}$$

$$= \begin{Bmatrix} \mathbf{Q}^{\text{std}} \\ F_s\big(\mathbf{Q}^{\text{enr}} + \mathbf{Q}_{cN}^{(m)}\big) + \mathbf{Q}_{cT}^{(m)} \end{Bmatrix} \tag{15}$$

with

$$\mathbf{K}_{uu} = \int_\Omega \mathbf{B}^T \mathbf{D} \mathbf{B} d\Omega \tag{16}$$

$$\mathbf{K}_{ua} = \int_\Omega \mathbf{B}^T \mathbf{D} \widetilde{\mathbf{B}} d\Omega \tag{17}$$

$$\mathbf{K}_{aa} = \int_\Omega \widetilde{\mathbf{B}}^T \mathbf{D} \widetilde{\mathbf{B}} d\Omega \tag{18}$$

$$\mathbf{K}_{cN} = 4k_N \int_{\Gamma_d^{\text{cont}}} \mathbf{N}^T \mathbf{n}_{\Gamma_d} \mathbf{n}_{\Gamma_d}^T \mathbf{N} d\Gamma \tag{19}$$

$$\mathbf{K}_{cT} = 4k_N \int_{\Gamma_d^{\text{cont}}} \tan\phi\, \mathbf{N}^T \mathbf{m}_{\Gamma_d} \mathbf{n}_{\Gamma_d}^T \mathbf{N} d\Gamma \tag{20}$$

$$\mathbf{Q}^{\text{std}} = \int_{\Gamma_t} \mathbf{N}^T \widetilde{\mathbf{t}} d\Omega + \int_{\Omega} \mathbf{N}^T \mathbf{b} d\Omega - \int_{\Omega} \mathbf{B}^T \boldsymbol{\sigma} d\Omega \tag{21}$$

$$\mathbf{Q}^{\text{enr}} = \int_{\Gamma_t} \widetilde{\mathbf{N}}^T \widetilde{\mathbf{t}} d\Omega + \int_{\Omega} \widetilde{\mathbf{N}}^T \mathbf{b} d\Omega - \int_{\Omega} \widetilde{\mathbf{B}}^T \boldsymbol{\sigma} d\Omega \tag{22}$$

$$\mathbf{Q}_{cN}^{(m)} = -2 \int_{\Gamma_d^{\text{cont}}} \mathbf{N}^T \mathbf{n}_{\Gamma_d} \widehat{\mathbf{N}} d\Gamma \mathbf{t}_N^{(m)} \tag{23}$$

$$\mathbf{Q}_{cT}^{(m)} = -2 \int_{\Gamma_d^{\text{cont}}} \tan\phi\, \mathbf{N}^T \mathbf{m}_{\Gamma_d} \widehat{\mathbf{N}} d\Gamma \mathbf{t}_N^{(m)} + 2 \int_{\Gamma_d^{\text{cont}}} c\mathbf{N}^T \mathbf{m}_{\Gamma_d} d\Gamma \tag{24}$$

where $\mathbf{D}$ = elastic matrix; and $\mathbf{Q}_{cN}^{(m)}$ and $\mathbf{Q}_{cT}^{(m)}/F_s$ = enrichment nodal forces induced by the normal and tangential tractions on Γ_d, respectively. The enrichment nodal forces are known in each augmentation iteration and updated according to Eq. (5).

As discussed earlier, there is no tangential displacement jump at the CUP. Therefore, by selecting the vital vertex (χ), the constraint of Eq. (6) can be expressed as follows:

$$k_N \mathbf{m}_{\Gamma_d}(\mathbf{x}_\chi) \mathbf{N}(\mathbf{x}_\chi) \overline{\mathbf{a}} \equiv \mathbf{K}_{\text{cup}} \overline{\mathbf{a}} = 0 \tag{25}$$

Finally, Eqs. (15) and (25) can be combined to form the following nonlinear equation:

$$\boldsymbol{\psi}^{(m)}(\mathbf{X}) = \begin{bmatrix} \mathbf{K}_{uu} & \mathbf{K}_{ua} & \\ F_s \mathbf{K}_{ua}^T & F_s(\mathbf{K}_{aa} + \mathbf{K}_{cN}) + \mathbf{K}_{cT} & \\ \mathbf{0} & \mathbf{K}_{\text{cup}} & \end{bmatrix} \begin{Bmatrix} \overline{\mathbf{u}}^{(m)} \\ \overline{\mathbf{a}}^{(m)} \end{Bmatrix}$$
$$- \begin{Bmatrix} \mathbf{Q}^{\text{std}} \\ F_s\left(\mathbf{Q}^{\text{enr}} + \mathbf{Q}_{cN}^{(m)}\right) + \mathbf{Q}_{cT}^{(m)} \\ 0 \end{Bmatrix} \tag{26}$$

where $\mathbf{X} \equiv \left\{\overline{\mathbf{u}}^T, \overline{\mathbf{a}}^T, F_s\right\}^T$ = unknown vector. Therefore, the safety factor (F_s) of the prescribed slip surface in the mth augmentation can be obtained by solving Eq. (26).

Other Issues Addressed in Proposed Method

Numerical Integration

In standard FEA, Gauss's integration is an effective approach to element integration. However, for elements bisected by a discontinuity, the enrichment function is different on each of the two sides of the discontinuity for the given enriched elements; clearly, in this condition, the original integration scheme cannot meet the precision requirement. Moreover, the stability analysis method proposed in this study must facilitate the CSS search, which requires the data structure of the elements to remain unchanged as the slip surfaces change.

The triangular mesh and the layout of Gauss's points in the enriched element presented in Fig. 3 are used. Normally, a triangular element is bisected by the discontinuity [zero level of $\varphi(\mathbf{x})$] into a triangle [Subtriangle 1 (ST1)] and a quadrangle, which can be further divided into two triangles (ST2 and ST3). Therefore, Gauss's points and their weights correspond to the centroids and areas of these three subtriangles [Fig. 3(a)]. The discontinuity must intersect the edges with nodes enriched as $H = 1$ and $H = -1$. Thus, even in
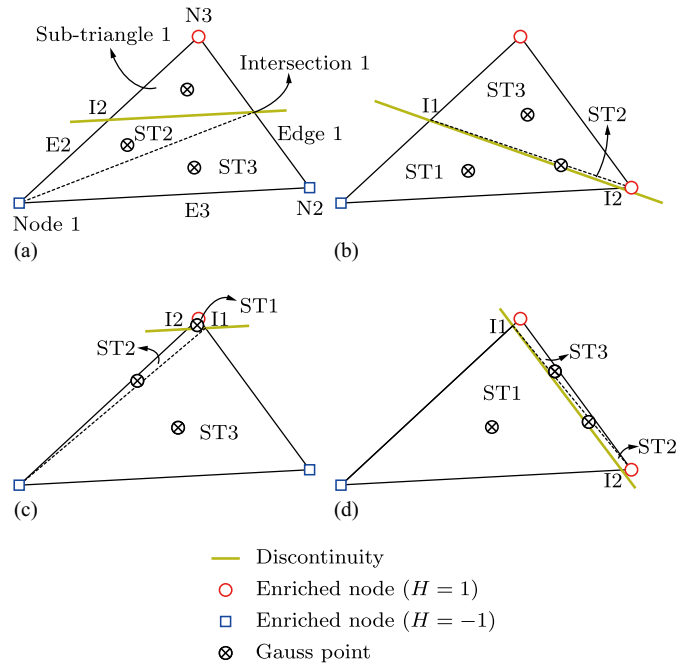

Fig. 3. Numerical integration of an enriched triangular element: (a) typical relationship between triangular element and discontinuity; (b) one of the intersections approaches a node, and area of ST2 is zero; (c) both intersections approach the same node, and areas of ST1 and ST2 are zero; and (d) two intersections approach different nodes, and areas of ST2 and ST3 are zero.

special cases in which one or two intersections may coincide with the nodes [Figs. 3(b–d)], Gauss's integration rule does not need to be changed if the areas of some subtriangles are zero. Therefore, the approach used to integrate over the enriched elements is unified. Moreover, because the derivation of the shape function of the triangular element is constant, $\widetilde{\mathbf{B}}(\mathbf{x})$ of each Gaussian point can be obtained by modifying $\mathbf{B}(\mathbf{x})$, which is a constant matrix.

In addition to integrating over the elements, it is necessary to integrate along Γ_d to obtain $\mathbf{K}_{cN}$, $\mathbf{K}_{cT}$, $\mathbf{Q}_{cN}$, and $\mathbf{Q}_{cT}$. As noted earlier, the VVT was used in this study, and the contact constraints were enforced at the vital vertices. For the normal penalization contributions ($\mathbf{K}_{cN}$ and $\mathbf{K}_{cT}$) along the discontinuity, the Gaussian quadrature method can be implemented based on the trapezoidal rule, with the integral points located at these vital vertices. Additionally, because the VVT is adopted, some enriched nodes may not be affected by the constraints along Γ_d. Therefore, to acquire the stable stress distribution on Γ_d, a two-order Gauss integration scheme with two integral points in each segment of Γ_d is adopted to determine $\mathbf{Q}_{cN}$ and $\mathbf{Q}_{cT}$. Thus, all enriched nodes have an equivalent nodal force generated by $\overline{\mathbf{t}}_N$.

Criteria for Suppression of Enriched DOFs of the Nodes

The diagonal elements in $\mathbf{K}_{aa}$ corresponding to enriched node I can be written as follows:

$$\mathbf{K}_{aaII} = \sum_{e \subset \Omega_I} \left[(1 - H_I)^2 \left(\mathbf{B}_I^e\right)^T \mathbf{D} \mathbf{B}_I^e A^{e+} \right]$$
$$+ \sum_{e \subset \Omega_I} \left[(-1 - H_I)^2 \left(\mathbf{B}_I^e\right)^T \mathbf{D} \mathbf{B}_I^e A^{e-} \right] \tag{27}$$

where e = element in Ω_I, which is the support region of node I; $\mathbf{B}_I^e$ = strain matrix of node I in element e; and A^{e+} and A^{e-} = areas of the

domains above and below the discontinuity in element e. When $H_I = 1$ and $A_I^- = \sum_{e \subset \Omega_I} A^{e-}$ is very small, $\mathbf{K}_{aaII} \ll \mathbf{K}_{uuII}$, where $\mathbf{K}_{uuII}$ represents the diagonal elements in $\mathbf{K}_{uu}$ corresponding to node I; similarly, when $H_I = -1$ and $A_I^+ = \sum_{e \subset \Omega_I} A^{e+}$ is very small, the same conclusion can be drawn.

The multiple orders of magnitude of the differences between $\mathbf{K}_{aaII}$ and $\mathbf{K}_{uuII}$ will lead to ill conditioning or even the singularity of the global stiffness matrix in XFEA. For node I with support region A_I, if the condition of $A_I^-/A_I < \Delta$ with $H_I = 1$ or $A_I^+/A_I < \Delta$ with $H_I = -1$ is satisfied, where Δ is the allowable tolerance, node I should not be enriched, as presented in Fig. 4. In practice, the tolerance (Δ) is usually set to 10^{-4}. In addition, instead of directly removing the enriched nodes that satisfy the aforementioned condition from $\mathcal{N}^{\text{enr}}$, as Dolbow (1999) and Khoei (2015) did, we force the enriched DOFs of these nodes to equal zero. Otherwise, a disparity in the data structure of the enriched elements will develop, and the algorithm complexity will increase.

Determination of CUP

The selection of the CUP for a potential slip surface was discussed in detail by Shi et al. (2017). Because the location of the CUP is not known a priori, it is necessary to perform a trial calculation to obtain the distribution of g_T on the slip surface by randomly selecting a point as the CUP; then, the node with the largest sliding distance is selected as the real CUP. Because $\mathbf{m}_{\Gamma_d}$ points in the direction opposite that of sliding, the tangential displacement jump (g_T) attributed to sliding is negative. However, a trial must be used to solve the nonlinear equations in Eq. (26), which will increase the computational cost. In most cases, the CUP is the point that has a maximum local FOS (F_a) on Γ_d, where $F_a = (t_N \tan\phi - c)/t_T$ and t_N and t_T are the initial rather than critical stress distributions on Γ_d. The point
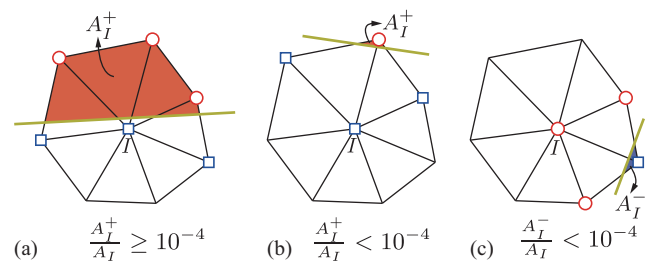

Fig. 4. Criterion for suppression of node enrichment: node I in (a) should be enriched, and node I in (b and c) does not need to be enriched.

with the maximum F_a value is typically the last to fail, which is similar to the definition of the CUP.

In this study, if the initial stress field of the slope was known, the strategy used to determine the CUP of a slip surface was as follows: (1) the CUP was estimated according to the distribution of the local FOS; (2) the CUP was verified with a trial; if the verification was successful, the result from the trial was the final result; otherwise, (3) to obtain the final result, the CUP was selected based on the distribution of g_T from the trial.

Solution of Nonlinear Equations

Newton's method is a classical and effective approach for solving a system of nonlinear equations, such as Eq. (26). An initial guess is set in the initial augmentation iteration with $\overline{\mathbf{u}}^0 = 0$, $\overline{\mathbf{a}}^0 = 0$, $F_s^0 = 1$, and $\mathbf{X}^0 = \{\mathbf{0}, 1\}^T$. Then, the derivative of $\psi(\mathbf{X})$ at $\mathbf{X}^n$ can be written as follows:

$$\psi'(\mathbf{X}^n) = \begin{bmatrix} \mathbf{K}_{uu} & \mathbf{K}_{ua} & \mathbf{0} \\ F_s^n \mathbf{K}_{ua}^T & F_s^n(\mathbf{K}_{aa} + \mathbf{K}_{cN}) + \mathbf{K}_{cT} & \mathbf{K}_{ua}^T \overline{\mathbf{u}}^n + (\mathbf{K}_{aa} + \mathbf{K}_{cN})\overline{\mathbf{a}}^n - \mathbf{Q}^{\text{enr}} - \mathbf{Q}_{cN}^{(m)} \\ 0 & \mathbf{K}_{\text{cup}} & \mathbf{0} \end{bmatrix} \quad (28)$$

A more accurate approximation is $\mathbf{X}^{n+1}$

$$\mathbf{X}^{n+1} = \mathbf{X}^n - \frac{\psi(\mathbf{X}^n)}{\psi'(\mathbf{X}^n)} \quad (29)$$

This process is repeated until the following condition is satisfied:

$$\eta_g = \frac{|\psi|}{|\{\mathbf{Q}_{\text{ext}}^{\text{std}}; \mathbf{Q}_{\text{ext}}^{\text{enr}}\}|} \le \eta_g^{\text{aim}} \quad (30)$$

In each augmentation loop, the nonlinear equations are solved by Newton's method with the initial guess from the last augmentation iteration. Because the guess is very close to the true solution, the convergence of Newton's iteration is very fast in subsequent augmentation iterations. The condition related to the convergence of the augmentation iteration is as follows:

$$\eta_l = \frac{1}{l^2} \int_{\Gamma_d^{\text{cont}}} |g_N| d\Gamma \le \eta_l^{\text{aim}} \quad (31)$$

where l = length of Γ_d^{cont}.

Normally, the determination of Γ_d^{cont} is based on the contact iteration, which is time-consuming. Therefore, to simplify the algorithm,

we determine Γ_d^{cont} according to the initial tensile stress distribution of the slope because a small area of opening is possible only at the rear edge of the slip surface. Moreover, the initial stress distribution on the slip surface is determined in standard FEA, and the stresses are discontinuous between elements. Here, the patch-based stress recovery technique (Zienkiewicz and Zhu 1992) was used to determine the stresses at the nodes; these stresses were then used to obtain the normal and tangential stresses at the vital vertices through the finite-element interpolation.

Because the limit-equilibrium condition, which is included in the critical unstable condition, is implemented in XFEA, we call this method of slope-stability analysis the X-FELE method. The algorithm flowchart of this approach is presented in Fig. 5. Notably, this method is easily combined with an optimization algorithm to locate the CSS. In the subsequent verification of the proposed X-FELE method, η_g^{aim} and η_l^{aim} are set to 10^{-6} and 10^{-12}, respectively.

Examples and Verification of X-FELE Method

The advantages of the FELE method over the traditional LEM, such as the ability to evaluate the influence of underground excavation
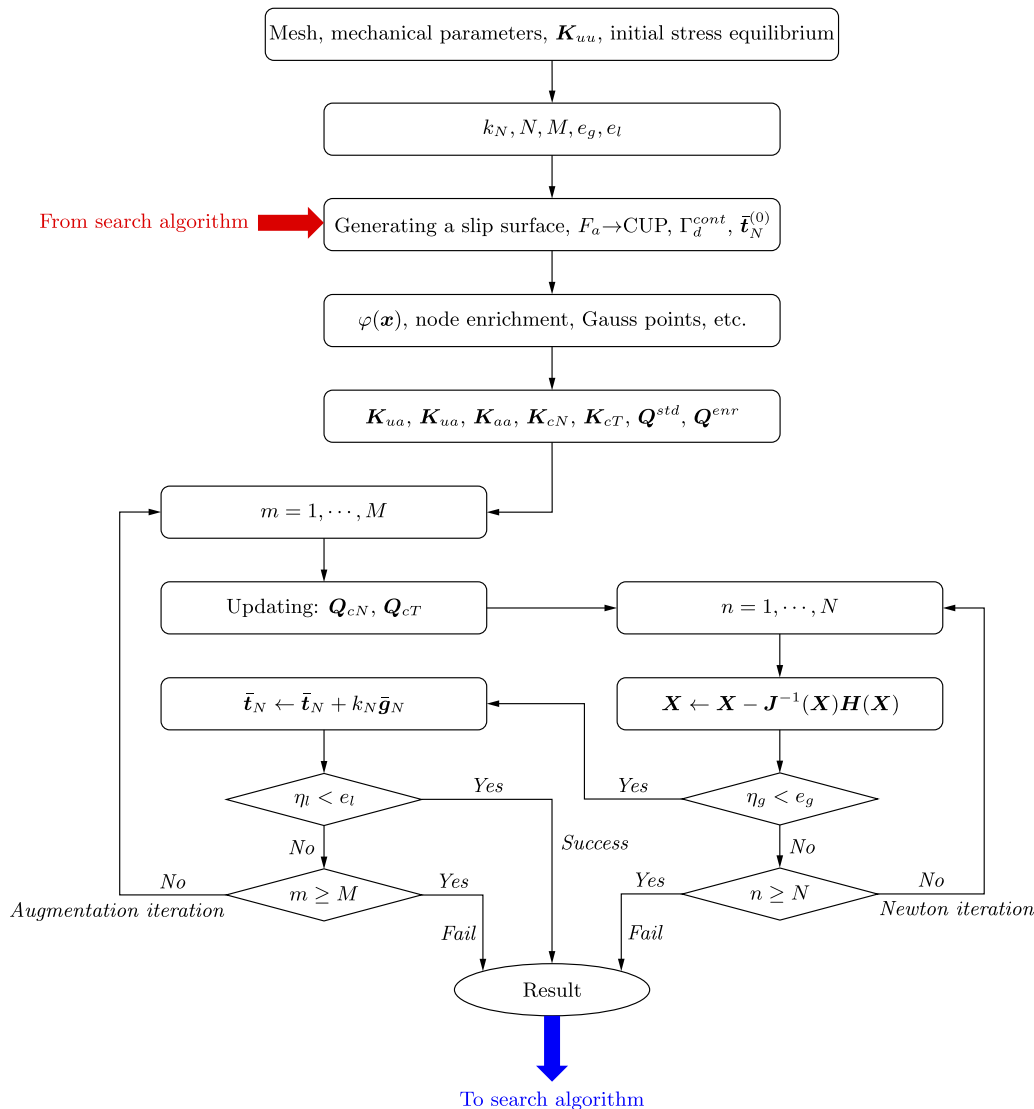
Fig. 5. Flow diagram of the implementation of the critical unstable conditions in XFEA.

on slope stability, have been demonstrated (Shi et al. 2017) and were not the focus of this study. Therefore, the following examples focus on the accuracy, convergence, and rationality of the stress distribution on the slip surface based on the use of XFEA in the proposed method.

Example 1: Planar Slip Surface

The first example is a planar slip surface with a FOS that can be analytically obtained. This example is used to verify the accuracy of the method of slope-stability evaluation. For a planar slip surface with an inclination angle of θ, the FOS can be expressed as follows:

$$F_s = \frac{\tan\phi}{\tan\theta} + \frac{lc}{V\gamma\sin\theta} \qquad (32)$$

where V = slip area in m³/m.

For simplicity, a 10×20-m rectangular region (plane-strain problem) that contained a planar slip surface was evaluated here. Fig. 6 presents the discretization of the region with a slip surface characterized by θ equal to 45°. The model material had an elastic

modulus (E) of 28 GPa, a Poisson's ratio (ν) of 0.23, and a unit weight (γ) of 27 kN/m³.

Table 1 presents a comparison of the FOS obtained by the analytical formula and the X-FELE method for the planar slip surface with different inclination angles. The proposed method had a very high computational accuracy. The following analysis was based on Case 4, as described in Table 1. For the planar slip surface with an inclination angle of 30°, the initial normal stress on the planar slip surface linearly decreased from left to right, as seen in Fig. 7. In this and the following examples, the compressive stress was positive. The graph of t_N versus the x-coordinate from the Morgenstern-Price method (MP) exhibited sinusoidal variation, which indicates that the interslice force assumption considerably influenced the distribution of the normal stress. Because the slip body or the entire slope was regarded as the deformable body and satisfied the deformation compatibility constraint, the normal stress obtained by the FELE method exhibited a different trend. Specifically, the stress first increased and then decreased from left to right. In this study, t_N from the FELE method (Fig. 7) was different from the result of Shi et al. (2017) because the entire slope was deformable. Most importantly, the results regarding the normal stress and FOS from the FELE and the proposed method were consistent. Thus, using the
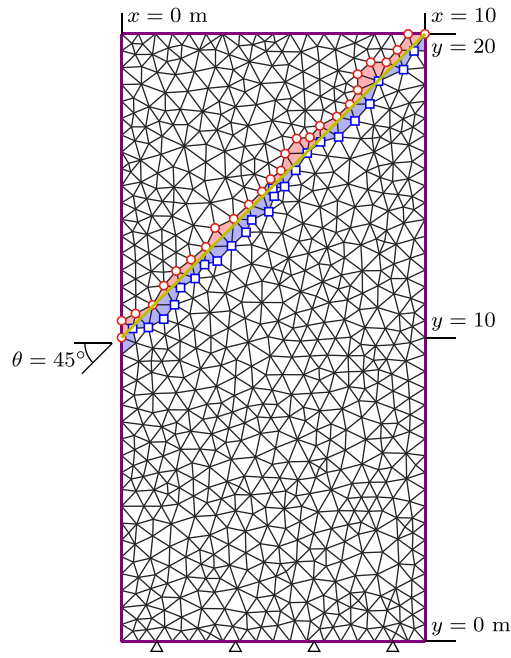
Fig. 6. Mesh with 747 nodes and 1,384 triangles for the planar slip surface example.

Table 1. Comparison of the FOS obtained from the analytical and proposed methods for the planar slip surface with different angles of inclination

Case	Strength parameters ϕ (°)	c (kPa)	Inclination angle θ (degrees)	F_s By Eq. (32)	X-FELE
1	35	0	30	1.212795	1.212795
2	35	0	35	1.000000	1.000000
3	35	0	45	0.700208	0.700208
4	30	20	30	1.592593	1.592593
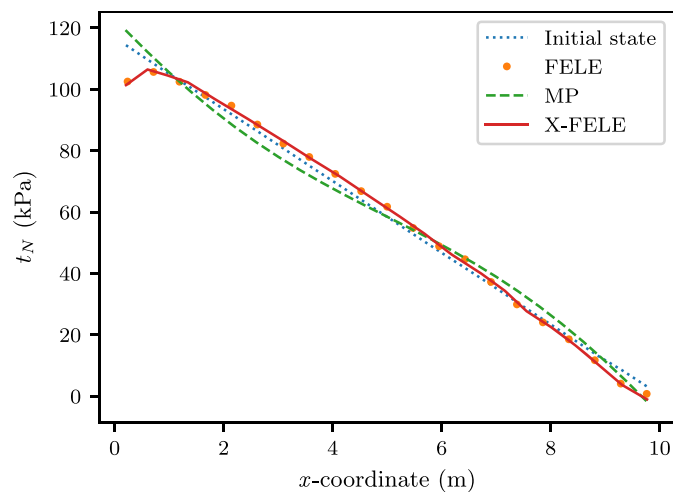
Fig. 7. Distributions of normal stress on the slip surface ($\theta = 30°$) obtained using different methods under the limit-equilibrium state when $\phi = 30°$ and $c = 20$ kPa; moreover, the initial normal stress is plotted for comparison. MP = Morgenstern-Price method.
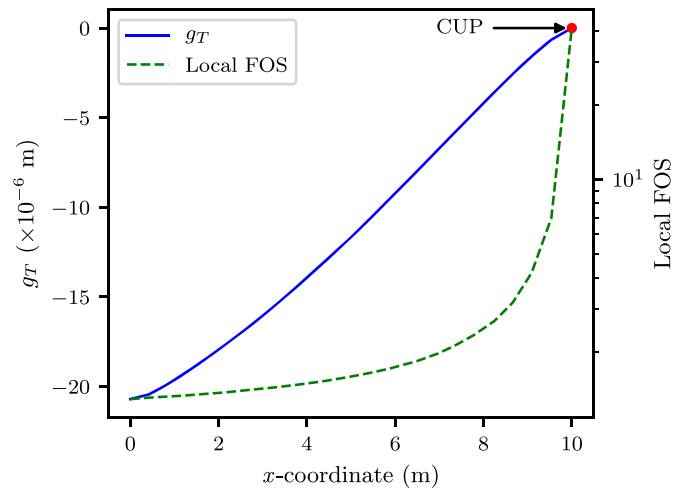
Fig. 8. Profiles of tangential displacement jump and local FOS along the planar slip surface.
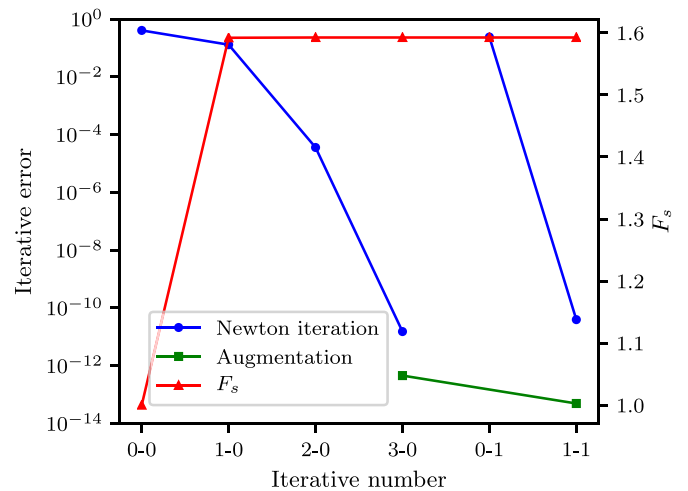
Fig. 9. Iterative information from the X-FELE method in the solution of Case 4 of Example 1; for the x-axis labels, i-m represents the ith Newton iteration within the mth augmentation iteration.

aforementioned methods to impose the critical unstable condition in XFEA was very effective, and the unreasonable oscillation of the stress distribution was largely corrected. Moreover, a smooth distribution of the stress on the slip surface can be obtained even if the slip surface is unevenly discretized based on an unstructured mesh.

The local FOS along the slip surface after gravity equilibrium was reached is presented in Fig. 8. Therefore, the right-most point on the slip surface with the highest local FOS was selected as the first candidate CUP. The tangential displacement jump of this point was expected to be the largest in the trial calculation. Therefore, the candidate CUP could be confirmed, and no further calculations were required. In addition, Fig. 8 shows that the larger the local FOS was, the smaller the amount of slippage was when the slip surface reached the critical unstable state.

The iterative information used to solve Case 4 is presented in Fig. 9, with $k_N = 5 \times 10^8$ MPa/m. Convergence was achieved in only three steps in the initial augmentation, illustrating that the rate of convergence of Newton's method was quadratic. Moreover,

using the solution from the previous augmentation step, which was close to the true solution, as the next initial guess, Newton's iteration converged in one step in the subsequent augmentation. In addition, with only one augmentation step, η_l decreased to 4.94×10^{-14}. After reducing the penalty parameter by 1 or 2 orders of magnitude, Case 4 was recalculated with the convergence profiles of the augmentation iteration listed in Table 2. When the penalty parameter was relatively conservative, the expected level of accuracy could still be achieved by the ALM, but the convergence rate was clearly reduced. Therefore, it was necessary to increase the value of the penalty parameter as much as possible without ψ' being ill conditioned. As a rule of thumb, k_N can be estimated by multiplying the largest diagonal element in $\mathbf{K}_{uu}$ and $\mathbf{K}_{aa}$ by 10^3 to 10^4.

Example 2: Circular Slip Surface

In 1988, a set of five basic slope-stability problems were distributed to both Australian and overseas geomechanic professionals as part of a survey sponsored by the Australian Computer-Aided Design Society (ACADS) for testing slope-stability programs (Donald and Giam 1992). Example 2 in this study was the ACADS EX1(c) problem for a three-layer slope. The soil properties are listed in Table 3, and the geometry and the discretization of this nonhomogeneous slope are presented in Fig. 10. A slip center search grid of 18×22 intervals was used, with 10 intervals between the maximum and minimum radii of the valid circles. The coordinates of the bottom-left and top-right corners of the search grid rectangle were (30, 36) and (43, 52) m, respectively. To constrain the allowable locations of the slip surfaces, two ranges for the starting and ending points were defined at the head and toe of the slope, respectively.

A total of 2,462 valid slip surfaces were assessed using the X-FELE, and their FOS are presented in Fig. 11. The CSS with a center located at (34.333, 42.545) m and a radius of 18.073 m had a FOS of 1.376, which is very close to the results obtained using the MP in the verification manual of the SLIDE software. Thus, the proposed method, which does not require mesh reconstruction, is suitable for use in the CSS search. Because the tangential stress exerted on the slip body at the edge of the CSS pointed in the sliding direction, the local FOS was negative. In this case, the CUP was selected among the points with negative local FOS. Of these points, that with a maximum sum of $|t_N|$ and $|t_T|$ can be selected as the CUP. As seen in Fig. 12, the CUP of the CSS was selected at the right-most point, which could be confirmed by the distribution of g_T along the CSS. In addition, the sliding distance of a point on the slip surface was negatively correlated with its antisliding ability. The displacement field of the slope when the CSS reached the critical unstable state is plotted in Fig. 13. The displacement of the middle of the sliding body was relatively large, and in combination with the g_T and local FOS distributions on the slip surface, it can be concluded that middle of the slip surface was the *weak link*.

As seen in Fig. 14, the difference in the normal stresses between the initial and critical unstable states was very small, and the difference between the tangential stresses in these states was relatively large. According to the tangential stress distribution, the endangered section of the slip surface, where the tangential stress under the initial state was greater than that under the critical unstable state, can be clearly determined. Moreover, the smooth distribution of the normal stress also reflected the robustness and effectiveness of the proposed method.

Example 3: Smooth Noncircular Surface

This example modeled Prandtl's well-known solution of the bearing capacity. The model of approximately 1,000 triangular elements is
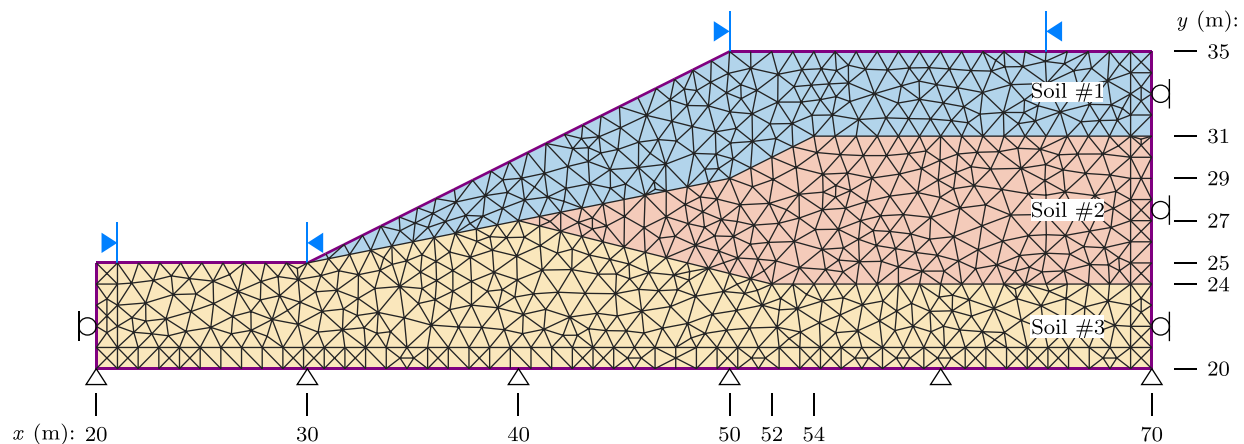
Table 2. Convergence profiles of augmentation iterations in the solution of Case 4 of Example 1 with different penalty parameters

Iterative number	$k_N^{(1)} = 5 \times 10^{14}$ MPa/m	$k_N^{(2)} = 0.1 k_N^{(1)}$	$k_N^{(3)} = 0.01 k_N^{(1)}$
0	4.58×10^{-13}	4.58×10^{-12}	4.58×10^{-11}
1	4.95×10^{-14}	4.95×10^{-13}	4.94×10^{-12}
2	—	2.94×10^{-13}	2.94×10^{-12}
3	—	1.91×10^{-13}	1.91×10^{-12}
4	—	1.26×10^{-13}	1.26×10^{-12}
5	—	8.33×10^{-14}	8.38×10^{-13}
6	—	—	5.57×10^{-13}
7	—	—	3.71×10^{-13}
8	—	—	2.47×10^{-13}
9	—	—	1.65×10^{-13}
10	—	—	1.10×10^{-13}
11	—	—	7.37×10^{-14}

Table 3. Soil properties of Example 2

Soil	c (kPa)	ϕ (degrees)	γ (kN/m^3)	E (kPa)	ν
1	0.0	38.0	19.5	1.0×10^4	0.25
2	5.3	23.0	19.5	1.0×10^4	0.25
3	7.2	20.0	19.5	1.0×10^4	0.25

Fig. 10. Geometry setup and discretization of Example 2. Mesh consisted of 1,426 triangles and 776 nodes.
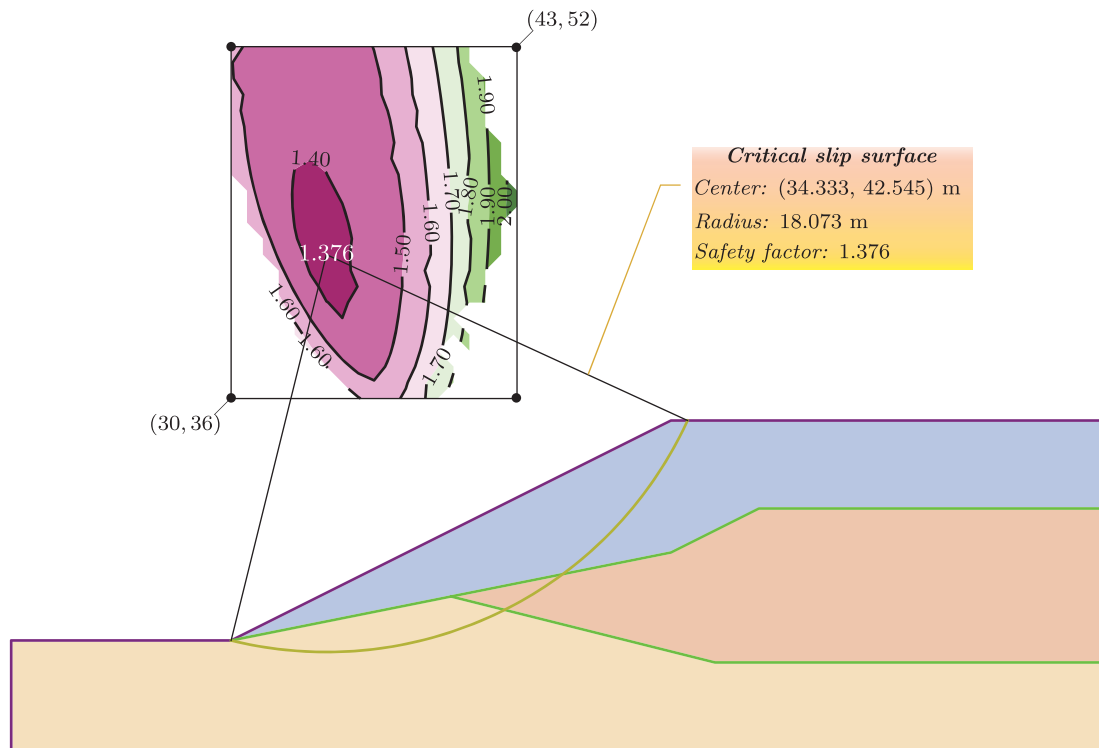
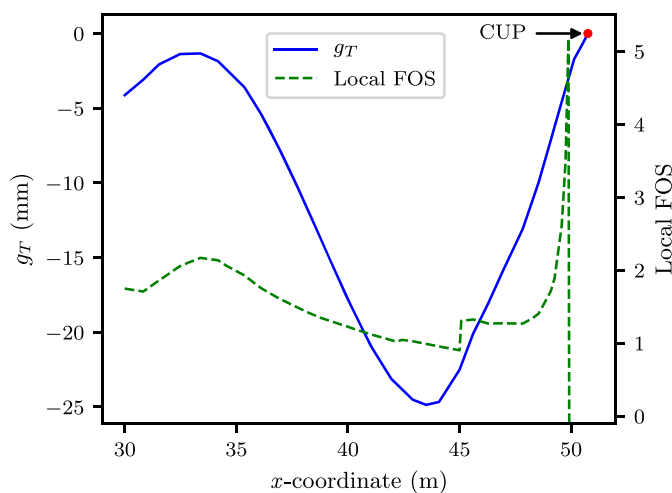**Fig. 11.** Grid search solution for Example 2 using the X-FELE method.

Fig. 12. Profiles of tangential displacement jump and local FOS along the CSS of Example 2.

shown in Fig. 15(a). The failure surface of the fan region was a quarter arc because the friction angle of the soil was zero. A uniformly distributed load of 102.83 kPa, which was Prandtl's solution of $q_c = 2c(1 + \pi/2)$, was applied over a width of 10 m, where $c = 20$ kPa. The Prandtl-type failure body can be divided into active, radial shear, and Rankine passive zones. Thus, failure must occur within the failure body. However, the X-FELE method cannot consider the plasticity of the slope, and the MP, rather than Prandtl's solution, was used for comparison. Moreover, this example was used to investigate the mesh sensitivity of the X-FELE method and the effect of the CUP selection on the results. The elastic modulus, Poisson's ratio, and unit weight of the soil were 50 MPa, 0.4, and 0, respectively.

To assess the mesh sensitivity of the proposed method, two additional meshes with approximately 500 and 2,000 elements, presented in Figs. 15(b and c), were constructed. The quality of these three meshes was generally poor. Under the action of the distributed load, the soil is compressed, and the CUP must be located at the right-most point of the failure surface, which is the last to fail. With this point as the CUP, the normal stress distributions and the sliding surface obtained by the X-FELE method using different meshes and the MP were plotted in Fig. 16(a). As can be observed, the normal stress distributions for different meshes were comparatively consistent. Note that the size of the contact element varied considerably due to the random intersection of the failure surface and the mesh, and it is difficult to achieve a completely uniform distribution using different meshes. Moreover, the FOS obtained by the X-FELE method using 500-element, 1,000-element, and 2,000-element meshes were 1.1260, 1.1232, and 1.1216, respectively, and the difference among them was less than 0.5%. Therefore, it can be concluded that the results of the X-FELE method were not sensitive to the mesh.

The FOS of the failure surface obtained by the MP was 0.94, which was approximately 16% smaller than that of the X-FELE method. The normal stress calculated by the MP was mainly distributed below the load, and this result was very different from that calculated by X-FELE. From the viewpoint of deformation compatibility, the normal stress obtained by the MP was unreasonable. Unlike the planar and circular slip surfaces, the FOS of this slip surface was extraordinarily sensitive to the normal stress distribution, even though the shear strength of the surface was independent of the normal stress because of the zero friction angle. In addition, as seen in Fig. 16(b), the normal stress distribution of the slip surface varied with the CUP location. The CUP located at the right-most, middle, and left-most portions of the failure surface corresponded to FOS of 1.1232, 1.0543, and 0.9808, respectively. This finding again confirmed that the normal stress distribution has a notable
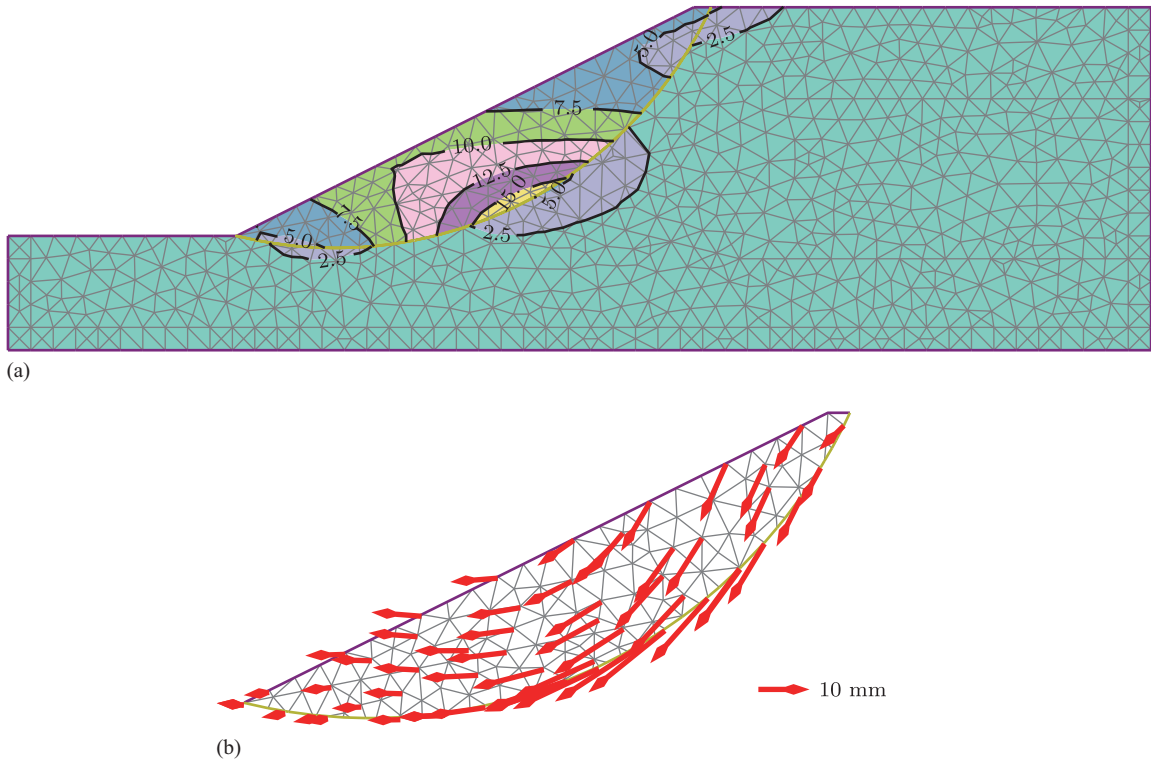
(a)

(b)

10 mm

Fig. 13. Displacement field with the CSS under the critical unstable state: (a) contours of displacement (contour labels are in mm); and (b) displacement direction of the slip body.
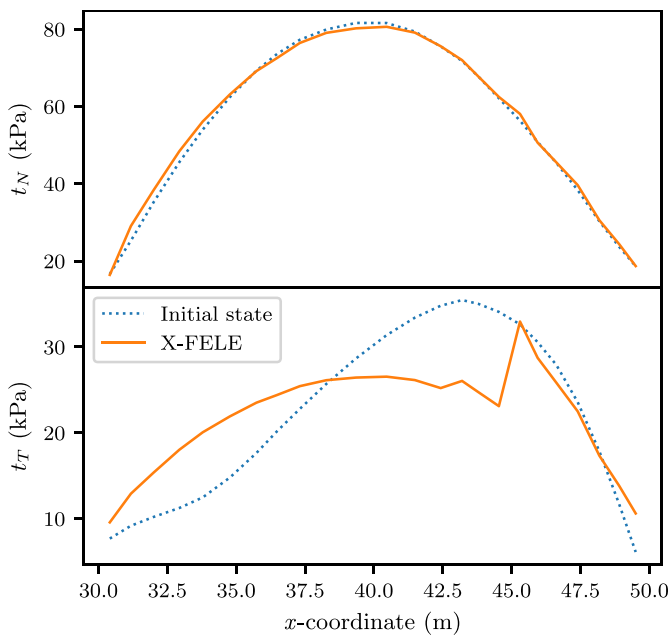

Fig. 14. Comparison of stress distributions of the CSS in initial and critical unstable states.

influence on the FOS. Therefore, CUP selection is critical in FELE calculations.

To introduce the supplementary condition of Eq. (8), any point on the slip surface can be selected as the CUP. The evolution of the
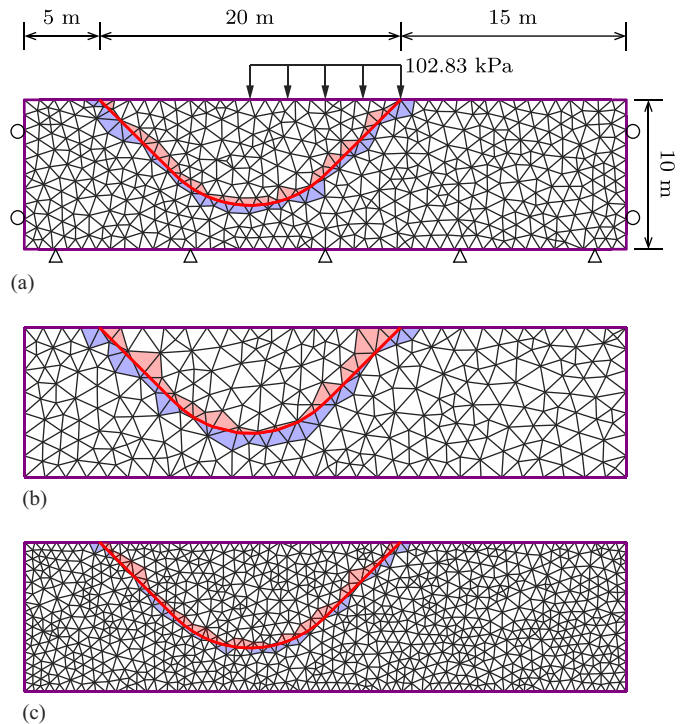
Fig. 15. Geometry setup, location of predefined slip surface, and boundary conditions together with discretization of Example 3: (a) mesh consisting of 933 triangles and 519 nodes; (b) mesh consisting of 506 elements and 290 nodes; and (c) mesh consisting of 1,796 elements and 973 nodes.
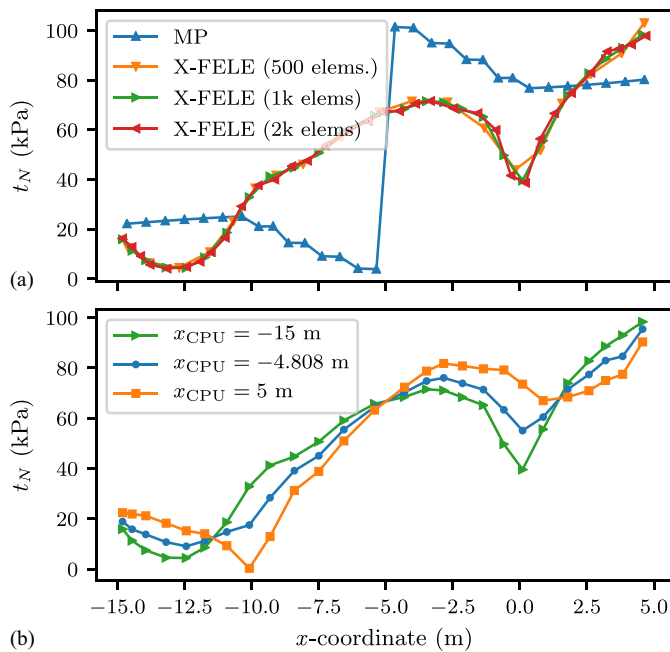
Fig. 16. Comparison of normal stress distributions along the slip surface for Example 3 obtained using (a) MP and X-FELE with a different density of mesh; and (b) X-FELE using a mesh of 1,000 elements with different CUPs.
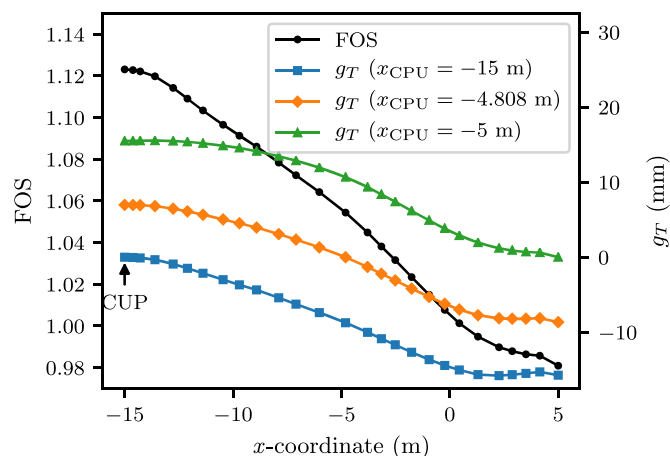

Fig. 17. FOS variation with the location of the CUP together with the distributions of the tangential displacement jump along the slip surface obtained using three different CUPs for Example 3.

FOS with the CUP location is presented in Fig. 17. According to Pan's extremum principle, the right-most point is the real CUP, which is consistent with the failure mechanism discussed earlier. This is a time-consuming method of determining the CUP. The CUP was determined according to the distribution of g_T on the slip surface in this study (i.e., g_T was largest at the CUP). The variation in g_T on the slip surface was generally the same regardless of which point was selected as the CUP, and this knowledge was the basis of the trial calculation strategy for determining the CUP. Thus, the selection of the CUP was in accordance with Pan's principle and conformed to the failure mechanism of the slip body. Determining the CUP based on the point with the largest local FOS is an estimation method that does not always succeed.

It should be emphasized that the proposed method should be developed further to include elastoplastic deformation and to study problems such as Example 3 more reasonably.

Conclusions

In this study, XFEA was used to establish the discrete form of the equilibrium equation with the critical unstable constraint of the pre-defined slip surface. To avoid oscillations, the VVT was used to stabilize the normal stress on the slip surface. The novelty of this study is that the slip surface was regarded as a discontinuity imbedded into the slope mesh, and the slope did not require remeshing for each slip surface. In addition, only the portion of the stiffness matrix that is related to the enriched DOFs must be reorganized. Therefore, the proposed method, called X-FELE, is suitable for locating the CSS due to the decrease in the computational burden associated with each slip surface. Three examples were solved to illustrate the accuracy and efficiency of the X-FELE. These analyses led to the following conclusions:

1. In the planar slip example, the FOS determined by the X-FELE method was equal to that of the analytical solution, which suggests that the X-FELE is highly accurate.
2. The smooth distribution of the normal stress on the planar and circular slip surfaces indicates that the X-FELE is robust for unstructured mesh configurations due to the implementation of the VVT.
3. The CUP can generally be determined by finding the point on the slip surface with the maximum local FOS, thereby reducing the computational cost by approximately half.
4. The ALM method can satisfy the normal constraint of the slip surface at a high level without strict penalty factor requirements.
5. The endangered section of the slip surface can be determined by comparing the tangential stress distributions in the initial and critical unstable states. Thus, the method can be used to help distinguish between landslide types.
6. The successful search for the CSS in Example 2 shows that the proposed method and the corresponding code aid in determining the FOS of a large number of predefined slip surfaces without changing the slope mesh.
7. The proposed method is insensitive to the mesh.

Acknowledgments

References

Bai, B., W. Yuan, and X. Li. 2014. "A new double reduction method for slope stability analysis." *J. Cent. South Univ.* 21 (3): 1158–1164. https://doi.org/10.1007/s11771-014-2049-6.

Belytschko, T., and T. Black. 1999. "Elastic crack growth in finite elements with minimal remeshing." *Int. J. Numer. Methods Eng.* 45 (5): 601–620. https://doi.org/10.1002/(SICI)1097-0207(19990620)45:5<601::AID-NME598>3.0.CO;2-S.

Bishop, A. W. 1955. "The use of the slip circle in the stability analysis of slopes." *Géotechnique* 5 (1): 7–17. https://doi.org/10.1680/geot.1955.5.1.7.

Brown, C. B., and I. P. King. 1966. "Automatic embankment analysis: Equilibrium and instability conditions." *Géotechnique* 16 (3): 209–219. https://doi.org/10.1680/geot.1966.16.3.209.

Budyn, É., G. Zi, N. Moës, and T. Belytschko. 2004. "A method for multiple crack growth in brittle materials without remeshing." *Int. J. Numer. Methods Eng.* 61 (10): 1741–1770. https://doi.org/10.1002/nme.1130.

Cheng, H., and X. Zhou. 2015. "A multi-dimensional space method for dynamic cracks problems using implicit time scheme in the framework of the extended finite element method." *Int. J. Damage Mech.* 24 (6): 859–890. https://doi.org/10.1177/1056789514555149.

Cheng, H., and X. Zhou. 2018. "New technique for frictional contact on crack slip in the extended finite-element method framework." *J. Eng. Mech.* 144 (8): 04018059. https://doi.org/10.1061/(ASCE)EM.1943-7889.0001476.

Cheng, Y. M., T. Lansivaara, and W. B. Wei. 2007. "Two-dimensional slope stability analysis by limit equilibrium and strength reduction methods." *Comput. Geotech.* 34 (3): 137–150. https://doi.org/10.1016/j.compgeo.2006.10.011.

Cheng, Y. M., and C. K. Lau. 2014. *Slope stability analysis and stabilization: New methods and insight.* 2nd ed. Boca Raton, FL: CRC Press.

Chin, E. B., J. B. Lasserre, and N. Sukumar. 2017. "Modeling crack discontinuities without element-partitioning in the extended finite element method." *Int. J. Numer. Methods Eng.* 110 (11): 1021–1048. https://doi.org/10.1002/nme.5436.

Daux, C., N. Moës, J. Dolbow, N. Sukumar, and T. Belytschko. 2000. "Arbitrary branched and intersecting cracks with the extended finite element method." *Int. J. Numer. Methods Eng.* 48 (12): 1741–1760. https://doi.org/10.1002/1097-0207(20000830)48:12<1741::AID-NME956>3.0.CO;2-L.

Dawson, E. M., W. H. Roth, and A. Drescher. 1999. "Slope stability analysis by strength reduction." *Géotechnique* 49 (6): 835–840. https://doi.org/10.1680/geot.1999.49.6.835.

de Vallejo, L. G., and M. Ferrer. 2011. *Geological engineering.* London: CRC Press.

Dolbow, J. E. 1999. "An extended finite element method with discontinuous enrichment for applied mechanics." Ph.D. thesis, Northwestern Univ.

Dolbow, J., N. Moës, and T. Belytschko. 2001. "An extended finite element method for modeling crack growth with frictional contact." *Comput. Methods Appl. Mech. Eng.* 190 (51–52): 6825–6846. https://doi.org/10.1016/S0045-7825(01)00260-2.

Donald, I. B., and P. Giam. 1992. "The ACADS slope stability programs review." In *Proc., 6th Int. Symp. on Landslides*, edited by D. H. Bell, 1665–1770. Rotterdam, Netherlands: A. A. Balkema.

Donald, I. B., and S. K. Giam. 1988. "Application of the nodal displacement method to slope stability analysis." In *Proc., Fifth Australia-New Zealand Conf. on Geomechanics: Prediction versus Performance; Preprints of Papers*, 456–460. Barton, Australia: Institution of Engineers Australia.

Eberhardt, E. 2003. "Rock slope stability analysis—Utilization of advanced numerical techniques." Accessed January 7, 2018. https://www.eoas.ubc.ca/personal/erik/e-papers/EE-SlopeStabilityAnalysis.pdf.

Fredlund, D. G., R. E. G. Scoular, and N. Zakerzadeh. 1999. "Using a finite element stress analysis to compute the factor of safety." In *Proc., 52nd Canadian Geotechnical Conf.*, 73–80. Richmond, BC, Canada: Canadian Geotechnical Society.

Fu, X., Q. Sheng, Y. Zhang, J. Chen, S. Zhang, and Z. Zhang. 2017. "Computation of the safety factor for slope stability using discontinuous deformation analysis and the vector sum method." *Comput. Geotech.* 92: 68–76. https://doi.org/10.1016/j.compgeo.2017.07.026.

Ge, X.-R. 2010. "The vector sum method: A new approach to calculating the safety factor of stability against sliding for slope engineering and dam foundation problems." *Advances in environmental geotechnics*, 99–110. New York: Springer.

Ge, X., D. Feng, and X. Gu. 1995. "Stability and deformation analysis of complex rock foundations of several large dams and hydropower stations in China." In *Proc., Int. Workshop on Rock Foundation*, 474–477. Tokyo: Balkema.

Giner, E., N. Sukumar, J. E. Tarancón, and F. J. Fuenmayor. 2009. "An Abaqus implementation of the extended finite element method." *Eng. Fract. Mech.* 76 (3): 347–368. https://doi.org/10.1016/j.engfracmech.2008.10.015.

Griffiths, D. V., and P. A. Lane. 1999. "Slope stability analysis by finite elements." *Géotechnique* 49 (3): 387–403. https://doi.org/10.1680/geot.1999.49.3.387.

Hirmand, M., M. Vahab, and A. R. Khoei. 2015. "An augmented Lagrangian contact formulation for frictional discontinuities with the extended finite element method." *Finite Elem. Anal. Des.* 107: 28–43. https://doi.org/10.1016/j.finel.2015.08.003.

Janbu, N. 1975. "Slope stability computations." *Int. J. Rock Mech. Min. Sci. Geomech. Abstr.* 12 (4): 67. https://doi.org/10.1016/0148-9062(75)90139-4.

Khoei, A. R. 2015. *Extended finite element method: Theory and applications.* Chichester, West Sussex: John Wiley & Sons.

Khoei, A. R., S. O. R. Biabanaki, and M. Anahid. 2009. "A Lagrangian-extended finite-element method in modeling large-plasticity deformations and contact problems." *Int. J. Mech. Sci.* 51 (5): 384–401. https://doi.org/10.1016/j.ijmecsci.2009.03.012.

Khoei, A. R., and M. Nikbakht. 2007. "An enriched finite element algorithm for numerical computation of contact friction problems." *Int. J. Mech. Sci.* 49 (2): 183–199. https://doi.org/10.1016/j.ijmecsci.2006.08.014.

Kim, J. Y., and S. R. Lee. 1997. "An improved search strategy for the critical slip surface using finite element stress fields." *Comput. Geotech.* 21 (4): 295–313. https://doi.org/10.1016/S0266-352X(97)00027-X.

Kulhawy, F. H. 1969. "Finite element analysis of the behavior of embankments." Ph.D. thesis, Univ. of California.

Liu, F., and R. I. Borja. 2009. "Finite deformation formulation for embedded frictional crack with the extended finite element method." *Int. J. Numer. Methods Eng.* 82 (6): 773–804.

Liu, S. Y., L. T. Shao, and H. J. Li. 2015. "Slope stability analysis using the limit equilibrium method and two finite element methods." *Comput. Geotech.* 63: 291–298. https://doi.org/10.1016/j.compgeo.2014.10.008.

Matsui, T., and K.-C. San. 1992. "Finite element slope stability analysis by shear strength reduction technique." *Soils Found.* 32 (1): 59–70. https://doi.org/10.3208/sandf1972.32.59.

Melenk, J. M., and I. Babuška. 1996. "The partition of unity finite element method: Basic theory and applications." *Comput. Methods Appl. Mech. Eng.* 139 (1–4): 289–314. https://doi.org/10.1016/S0045-7825(96)01087-0.

Moës, N., E. Béchet, and M. Tourbier. 2006. "Imposing Dirichlet boundary conditions in the extended finite element method." *Int. J. Numer. Methods Eng.* 67 (12): 1641–1669. https://doi.org/10.1002/nme.1675.

Moës, N., J. Dolbow, and T. Belytschko. 1999. "A finite element method for crack growth without remeshing." *Int. J. Numer. Methods Eng.* 46 (1): 131–150. https://doi.org/10.1002/(SICI)1097-0207(19990910)46:1<131::AID-NME726>3.0.CO;2-J.

Morgenstern, N. R., and V. E. Price. 1965. "The analysis of the stability of general slip surfaces." *Géotechnique* 15 (1): 79–93. https://doi.org/10.1680/geot.1965.15.1.79.

Naylor, D. J. 1982. "Finite elements and slope stability." *Numerical methods in geomechanics*, edited by J. B. Matrins, 229–244. New York: Springer.

Pham, H. T. V., and D. G. Fredlund. 2003. "The application of dynamic programming to slope stability analysis." *Can. Geotech. J.* 40 (4): 830–847. https://doi.org/10.1139/t03-033.

Shi, L., B. Bai, and X. Li. 2017. "Stability analysis of prescribed slip surfaces based on a combination of the equilibrium equation and the critical unstable condition." *Int. J. Geomech.* 17 (12): 04017118. https://doi.org/10.1061/(ASCE)GM.1943-5622.0001034.

Shi, L., X. Li, W. Ren, and Z. Fang. 2009. "Hybrid of ant colony algorithm and genetic algorithm and its application to searching critical slope slip surface." [In Chinese.] *Rock Soil Mech.* 30: 3486–3492.

Shi, L., X. Li, G. Sun, and B. Bai. 2012. "Research on stability of open-mining slope under underground mining." [In Chinese.] *Rock Soil Mech.* 33: 812–820.

Shi, L., and T. Yu. 2014. "Analysis of multiple crack growth using extended finite element method." [In Chinese.] *Rock Soil Mech.* 35 (1): 263–272.

Simo, J. C., and T. A. Laursen. 1992. "An augmented Lagrangian treatment of contact problems involving friction." *Comput. Struct.* 42 (1): 97–116. https://doi.org/10.1016/0045-7949(92)90540-G.

Spencer, E. 1967. "A method of analysis of the stability of embankments assuming parallel inter-slice forces." *Géotechnique* 17 (1): 11–26. https://doi.org/10.1680/geot.1967.17.1.11.

Sukumar, N., N. Moës, B. Moran, and T. Belytschko. 2000. "Extended finite element method for three-dimensional crack modelling." *Int. J.*

Numer. Methods Eng. 48 (11): 1549–1570. https://doi.org/10.1002/1097-0207(20000820)48:11<1549::AID-NME955>3.0.CO;2-A.

Ventura, G., E. Budyn, and T. Belytschko. 2003. "Vector level sets for description of propagating cracks in finite elements." *Int. J. Numer. Methods Eng.* 58 (10): 1571–1592. https://doi.org/10.1002/nme.829.

Wang, W., W. Yuan, X. Li, and B. Bai. 2016. "Evaluation approach of the slope stability based on deformation analysis." *Int. J. Geomech.* 16 (2): 04015054. https://doi.org/10.1061/(ASCE)GM.1943-5622.0000528.

Zheng, H., D. F. Liu, and C. G. Li. 2005. "Slope stability analysis based on elasto-plastic finite element method." *Int. J. Numer. Methods Eng.* 64 (14): 1871–1888. https://doi.org/10.1002/nme.1406.

Zhou, X., and H. Cheng. 2017. "Multidimensional space method for geometrically nonlinear problems under total Lagrangian formulation based on the extended finite-element method." *J. Eng. Mech.* 143 (7): 04017036. https://doi.org/10.1061/(ASCE)EM.1943-7889.0001241.

Zhou, X., and H. Yang. 2012. "Multiscale numerical modeling of propagation and coalescence of multiple cracks in rock masses." *Int. J. Rock Mech. Min. Sci.* 55: 15–27. https://doi.org/10.1016/j.ijrmms.2012.06.001.

Zienkiewicz, O. C., C. Humpheson, and R. W. Lewis. 1975. "Associated and non-associated visco-plasticity and plasticity in soil mechanics." *Géotechnique* 25 (4): 671–689. https://doi.org/10.1680/geot.1975.25.4.671.

Zienkiewicz, O. C., and J. Z. Zhu. 1992. "The superconvergent patch recovery and a posteriori error estimates. Part 1: The recovery technique." *Int. J. Numer. Methods Eng.* 33 (7): 1331–1364. https://doi.org/10.1002/nme.1620330702.